Investigation of convective transport in the gas diffusion layer used in polymer electrolyte fuel cells

Otávio Beruski,[1,*] Thiago Lopes,[1,2,†] Anthony R. J. Kucernak,[2,‡] and Joelma Perez[1,§]
[1]*Instituto de Química de São Carlos, Universidade de São Paulo, 13566-590 São Carlos, São Paulo, Brazil*
[2]*Department of Chemistry, Imperial College London, South Kensington Campus, London SW7 2AZ, United Kingdom*
(Received 6 April 2017; published 17 October 2017)

Recent experimental data on a fuel-cell-like system revealed insights into the fluid flow in both free and porous media. A computational model is used to investigate the momentum and species transport in such a system, solved using the finite element method. The model consists of a stationary, isothermal, diluted species transport in free and porous media flow. The momentum transport is treated using different formulations, namely, Stokes-Darcy, Darcy-Brinkman, and hybrid Stokes-Brinkman formulations. The species transport is given by the advection equation for a reactant diluted in air. The formulations are compared to each other and to the available experimental data, where it is concluded that the Darcy-Brinkman formulation reproduces the data appropriately. The validated model is used to investigate the contribution of convection in reactant transport in porous media of fuel cells. Convective transport provides a major contribution to reactant distribution in the so-called diffusion media. For a serpentine channel and flow with Re = 260–590, convection accounts for 29–58% of total reactant transport to the catalyst layer.

DOI: 10.1103/PhysRevFluids.2.103501

I. INTRODUCTION

Despite the great promise and effort involving the commercialization and deployment of fuel cell technologies, several issues remain to be understood before one can say that control over these systems has been achieved [1]. Different approaches are being explored, and one such approach involves the use of computer models to assist in the interpretation of experimental data and possibly to predict optimum design and conditions. Indeed, great effort has been seen in the development of *ab initio* and semiempirical models for fuel cell systems, as exemplified by the compiled data and references in Refs. [2–5] and, more recently, in Ref. [1]. These works evidently point out the amount of work still needed to be done in theoretical, computational, and experimental approaches but also highlight the benefits of coupling these, and the need to do so.

As pointed out by Weber *et al.* [1], modeling is heavily dependent on experimental results, from the input parameters to insights related to the mathematical description of physical phenomena that may occur in the experimental device. Therefore, validation is extremely important in order to ensure that the model complies with the physical effects observed in reality, both locally and globally. That being said, the desired *in situ* data are remarkably difficult to obtain reliably. The impressive degree of variability in design, operational conditions, and experimental systems turns the validation into a problem by itself, given that, usually, only part of the measurements and properties are experimentally available for specific devices. In fact, for complex, multiphysics systems, such as

[*]Present address: Nuclear and Energy Research Institute, IPEN/CNEN-SP, 05508-000 São Paulo, São Paulo, Brazil; oberuski@alumni.usp.br
[†]Present address: Nuclear and Energy Research Institute, IPEN/CNEN-SP, 05508-000 São Paulo, São Paulo, Brazil; tlopeschem@gmail.com
[‡]anthony@imperial.ac.uk
[§]jperez@iqsc.usp.br

fuel cells, one would hope to validate each aspect of the mathematical approach used, independently; however, results to allow for such independent assessments are rare.

Recently a promising experimental setup to allow probing and *in situ* observation of fluid flow in fuel-cell-like systems was published by some of us [6]. This approach used an allotrope of oxygen to mimic the flow of oxygen through a fuel cell replica. In this case, ozone (O_3) diluted in air was used as tracer, and a coumarin-based dye was used as the sensor to map the local concentration of O_3. The O_3 interacts with the dye in a porous layer, similarly to dioxygen and a metal- or carbon-based catalyst layer in a fuel cell, resulting in the emission of photons and the degradation of both reactant and catalyst. Measuring the light emission from this "catalyst layer" allowed determination of the local O_3 concentration and, thus, the flow dynamics in a system very similar to a fuel cell cathode operating in a regime in which flooding does not occur. It was proposed that, contrary to what is usually assumed, convection plays a significant role in the distribution of reactants in the porous layers. The unique data reported in Ref. [6] are welcome amidst a gap in research of such aspects in the field, providing an opportunity to further refine computational models for fuel-cell-like systems, enabling the validation of momentum and species transport in both global and local aspects.

As reported in the review by Weber and Newman [2], the majority of fuel cell models treat species transport in the porous domains solely by diffusion, with some models coupling it to Darcy's law. In 2014, Weber *et al.* [1] stated that the usual approach for momentum transport modeling is through Navier-Stokes equations coupled to Darcy's law, sometimes called the Stokes-Darcy (SD) formulation. Indeed, it is seen that the SD formulation is widely used in fuel cell models (e.g., as described by Rawool and co-workers [7] and more recently described in Ref. [8]) and also for related systems (for instance, the work of Knehr and collaborators in vanadium flow cells [9]). On the other hand, there are systems that do not necessarily make use of porous media. The work of Braff and colleagues [10] is such an example, studying membraneless flow cells. The authors study convection through boundary layer analysis, deriving analytical equations for fast examination of experimental systems. The correct description of momentum transport is, particularly in this case, essential to properly account for species transport.

It is underappreciated, though, that in order to couple the velocity fields near the interface between the free and porous domains it is necessary to introduce appropriate boundary conditions. Two such interfacial models are compared by Le Bars and Worster [11], namely, one from Beavers and Joseph [12] and another proposed by the authors, where the latter is shown to be more accurate. An alternative to the SD formulation is the so-called Darcy-Brinkman (DB) formulation [11], where both free and porous media flow are treated simultaneously, therefore eliminating the need for an explicit boundary condition for the velocity field near the interface. It can also be shown that the DB formulation reverts to the SD formulation as the permeability approaches zero, or as particle size becomes very large, making it a more general approach [11]. In fact, the boundary conditions discussed in Ref. [11] are compared to the DB formulation in order to assess its accuracy. In light of this, one would expect the DB formulation to be preferable for momentum transport modeling in fuel cells; however, it seems that no thorough validation of its use in these systems has been made, and few works have been found to actually use it [13,14]. On the other hand, the wide range of length scales known to exist in fuel cells favors the multiple-domain SD approach, allowing for a better description of the flow variables in each domain. In this case, the correct choice of interfacial boundary conditions should be important for fuel cell modeling.

In order to explore the differences between the outlined approaches, a macroscopic, finite-element-based model was assembled to simulate the species and flow dynamics of the system reported in Ref. [6]. Using the available data to validate the approach, the intent is to assist in the understanding of the system and, ultimately, jointly provide a consistent tool to study the dynamics of fuel-cell-like systems. The remainder of this work is organized as follows. The mathematical formulations used in the model are presented in Sec. II, along with remarks regarding the geometry and parameters used in the simulations. In Sec. III, the model is compared to the available experimental data in order to choose a suitable, validated formulation. The validated model is then used to assess the hypothesis raised in the experimental work, providing a discussion regarding the existence, or not, of postulated

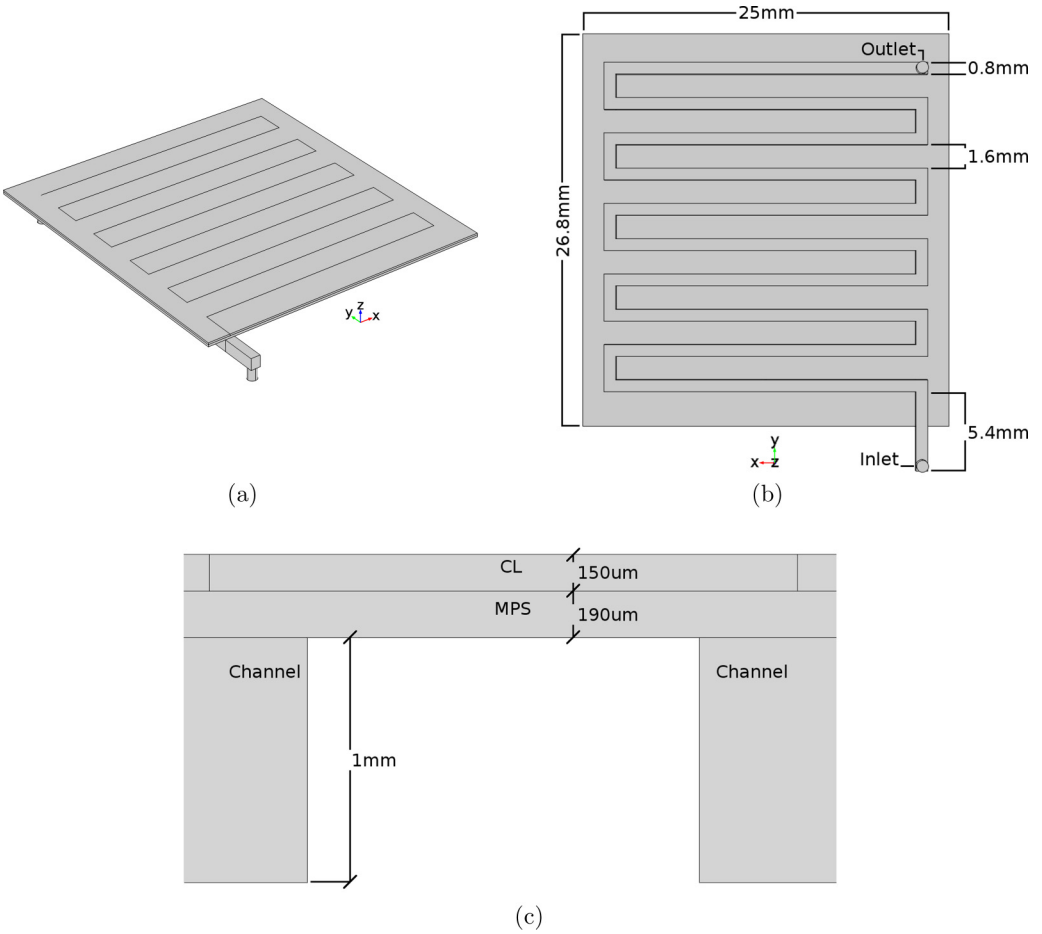

FIG. 1. Geometry used in the model: (a) upper view of the full geometry, showing the middle-channel projection on the CL, (b) downside view showing flow channel geometry, and (c) cross section view of (b), showing the porous media domains. From top to bottom: catalyst layer, macroporous substrate, and flow channels.

phenomena in the reported system and its implications in an actual fuel cell. Section IV presents the final remarks and perspectives to this work.

II. METHODS

All finite element calculations were performed using the commercial software COMSOL MULTIPHYSICS 5.1, along with the CFD, and Batteries and Fuel Cell modules. Unless otherwise noted, default parameters are assumed. The mathematical framework used was recently revised by Weber *et al.* [1] for fuel cell systems, and a detailed description may be found in Ref. [1] and references therein, while Le Bars and Worster [11] provide a derivation and discussion regarding the Darcy-Brinkman formulation and the interface boundary conditions. Details regarding the implementation may be found in the software's reference manual [15] and the modules' user guides [16,17]. The remaining data manipulation was performed using the R2012a version of MATLAB.

The geometry used for the simulations follows the one reported for the experimental apparatus [6] and is presented in Fig. 1: A single-channel serpentine geometry was used for the flow channel geometry; a porous layer for the diffusion media, representing the macroporous carbon paper

substrate (MPS); and finally a silica gel based catalytic layer (CL), where the catalyst is assumed homogeneously distributed. The CL includes a surface that follows the middle of the flow channel projection, crossing the entire CL domain thickness, used for probing the model [Fig. 1(a)]. No compression was assumed for the thicknesses of the porous media.

The level of theory used is that of stationary, isothermal transport of diluted species, consisting of O_3 diluted in air, coupled to free and porous media fluid flow. The chemical species transport is modeled by the diffusion-advection equation, defined in all domains:

$$\nabla \cdot \left(- D_{O_3} \nabla C_{O_3} \right) + (\mathbf{u} \cdot \nabla) C_{O_3} = R_{O_3} \tag{1}$$

along with the definition of the species flux vector,

$$\mathbf{N}_{O_3} = -D_{O_3} \nabla C_{O_3} + \mathbf{u} C_{O_3} \tag{2}$$

Here, D is the diffusion coefficient of the species, C is the concentration, $\mathbf{u}$ is the flow velocity vector, and R is the total reaction, source or sink, term. Since a dilute mixture is assumed, the diffusion is given by Fick's law.

The momentum transport follows three major mathematical frameworks: (i) SD, (ii) DB, or (iii) a mixed Stokes-Brinkman (SB) formulation. The SD approach consists of the compressible formulation of the Navier-Stokes equation,

$$\rho(\mathbf{u} \cdot \nabla)\mathbf{u} = \nabla \cdot \left[-P\mathbf{I} + \mu(\nabla \mathbf{u} + (\nabla \mathbf{u})^{\mathrm{T}}) - \tfrac{2}{3}\mu(\nabla \cdot \mathbf{u})\mathbf{I} \right], \tag{3}$$

defined in the flow channel domain, and Darcy's law,

$$\mathbf{u} = -\frac{\kappa}{\mu} \nabla P, \tag{4}$$

for the porous media domains. Here, ρ is the density of the fluid, P is the pressure, μ is the viscosity of the fluid, κ is the porous medium permeability, and $\mathbf{I}$ is the identity matrix. It should be noted that for Darcy's law, the velocity $\mathbf{u}$ is actually given by the Darcy velocity, which corresponds to the discharge rate per unit area. The DB formulation consists of a single equation, defined in all domains:

$$\frac{\rho}{\epsilon}(\mathbf{u} \cdot \nabla)\left(\frac{\mathbf{u}}{\epsilon}\right) = \nabla \cdot \left[-P\mathbf{I} + \frac{\mu}{\epsilon}(\nabla \mathbf{u} + (\nabla \mathbf{u})^{\mathrm{T}}) - \frac{2\mu}{3\epsilon}(\nabla \cdot \mathbf{u})\mathbf{I} \right] - \frac{\mu}{\kappa}\mathbf{u}, \tag{5}$$

where ϵ is the porosity. The SB approach consists of using the Navier-Stokes equation for free flow, while using Eq. (5) solely for the porous media domains. Regardless of the formulation used, the continuity equation is also defined on all domains:

$$\nabla \cdot (\rho \mathbf{u}) = 0, \tag{6}$$

where no momentum source or sink terms were used.

The full dilute species transport includes inflow and outflow conditions at the inlet and outlet, respectively [Fig. 1(b)]. The effective diffusion coefficient, in the porous layer domains, was given by

$$D_{\mathrm{eff}} = f_{\mathrm{eff}} D, \tag{7}$$

where f_{eff} was calculated using the tortuosity model $f_{\mathrm{eff}} = \epsilon/\tau$, in the MPS, and the Bruggeman model $f_{\mathrm{eff}} = \epsilon^{3/2}$, for the CL. The reaction term in Eq. (1) was defined for the O_3 in the CL, representing the first-order reaction with the catalyst,

$$R_{O_3} = -k C_{O_3}, \tag{8}$$

where k is the apparent reaction rate constant. A no-flux condition was used in all remaining, outer surfaces, and the initial values for the O_3, in all domains, follows the inflow concentration of 1200 ppm.

For the momentum transport, the density and viscosity were assumed to be the same as that of dry air at $T = 298$ K, neglecting the presence of O_3. The porous layers are assumed isotropic and

TABLE I. Parameters used in the model.

Parameter	Value	Ref.
O_3 diffusion coefficient in N_2, D_{O_3}	0.16 $cm^2\ s^{-1}$	[22,23]
O_3-coumarin reaction rate constant, k	250 s^{-1}	see text
Reference pressure, P_{ref}	1.027 bar	see text
Cell back pressure, P_{out}	1.0994 bar − P_{ref}	see text
Carbon paper porosity, ϵ_{MPS}	0.801	[24]
Carbon paper permeability, κ_{MPS}	9.18×10^{-12} m^2	[25]
Carbon paper tortuosity, τ_{MPS}	1.199	[25]
Catalyst layer porosity, ϵ_{CL}	0.497	see text
Catalyst layer permeability, κ_{CL}	8.82×10^{-11} m^2	see text

are characterized using the porosity and permeability of the material. The inlet condition was given by a normal inflow velocity, defined by the flow rate Q, over the inlet area A_{in}:

$$\mathbf{u} \cdot \mathbf{n} = Q/A_{in} \tag{9}$$

with $\mathbf{n}$ being the vector normal to the inlet surface, and Q ranging from 200 to 450 $cm^3\ min^{-1}$. The outlet was defined by a constant pressure, with suppression of backflow, the value of it being supplied by the authors of Ref. [6]. To allow comparison with different systems, the Reynolds number was calculated using Q, the average kinematic viscosity over the entire flow channel domain, and the hydraulic diameter for rectangular channels, assuming the MPS as a solid wall. The remaining surfaces were all subjected to a no-slip condition. The initial values used were $\mathbf{u} = 0$ and $P = 0.01$ bar, and all simulations were subjected to a reference pressure P_{ref}, provided by the authors of Ref. [6].

For the SD and SB formulations, several setups were tested in order to implement the interface boundary conditions described in Ref. [11]. Little or no difference was seen when comparing the setups (Figs. S1–S4 in the Supplemental Material (SM) [18]). The chosen setups, for comparison with the DB formulation, include a slip velocity for the free flow field at the interface between the channel and MPS domains:

$$\mathbf{u} = \frac{L_s}{\mu}\tau_{n,t}, \tag{10}$$

where L_s is the slip length, and $\tau_{n,t}$ is the tangential shear stress at the boundary. The slip length is given by the following [11]:

$$L_s = c\sqrt{\frac{\kappa}{\epsilon}}, \tag{11}$$

where c is an adjustable constant, taken as unity in this case. For the MPS domain, unlike the proposed continuity condition for the flow field given in Ref. [11], only the pressure resulting from the free flow in the interface was considered in either formulation. This is the same as the interpretation of the Beavers-Joseph interfacial condition given by Le Bars and Worster [11]. The remaining setups investigated for the SD and SB formulations are described in the SM [18].

The parameters used for the simulations are specified in Table I. Not all were available, for instance, the physical properties for the CL, which were estimated as follows: Data regarding the size distribution of the silica particles used were taken from the manufacturer (Nano Silica Gel, Sigma Aldrich), reported to be between 6.0 and 9.0 μm, and then used in a simulation of a permeability experiment to estimate the porosity and permeability. Spherical particles, with the mentioned particle range, were randomly distributed in a 1 mm width, 150 μm thick, bidimensional bed, without superposition, and subjected to a flow with Reynolds number ranging from 0.1 to 1. The bed pressure drop, assumed linear, was plotted against the total discharge rate and then fitted to the Darcy-Forchheimer equation [21] to provide the permeability, where the porosity was evaluated

from the void area in the bed. The procedure was repeated ten times, and the values reported in Table I are the average values. Also not available was the reaction rate constant for the O_3 reaction with the catalyst used in the experiments (7-diethylamino-4-methylcoumarin [6]):

$$O_3 + (C_2H_5)_2NC_9H_6O_2CH_3 \rightarrow \text{Products} + h\nu. \tag{12}$$

It was, therefore, varied between 10^1 and 10^3 s^{-1} and was chosen to better describe, qualitatively, the partial pressure surfaces reported by Lopes *et al.* (Fig. 5 of Ref. [6]).

Finally, the mesh used for the computations was generated using a predefined "finer" triangular mesh on all outer surfaces (minimum and maximum element sizes 3.06×10^{-5} and 2.83×10^{-4} m, respectively; maximum element growth rate 1.1; curvature factor 0.4; and resolution in narrow regions, 0.9), with corner refinement (element size scaling factor 0.35), and the domains were filled with a "coarse" tetrahedral mesh (minimum and maximum element sizes 2.29×10^{-4} and 7.65×10^{-4} m, respectively; maximum element growth rate 1.2; curvature factor 0.7; and resolution in narrow regions, 0.7), with three quadrilateral elements being included in the direction normal to the flow channels walls ("boundary layer" elements). The final mesh has element sizes ranging from 2.03×10^{-5} to 3.45×10^{-4} m, with an average element quality of 0.5432, totalling $\sim 1.7 \times 10^6$ domain elements. The system was solved for the stationary state, using a segregated, two-step approach: first the flow variables, then the O_3 concentration. All variables had linear discretization. Each step was solved using an implementation of the PARDISO linear solver, with a relative tolerance of 10^{-3}, and with scaling based on the initial values. A parametric sweep was used to solve for the inlet flow rate values, with a step of 50 $cm^3\,min^{-1}$, with each previous solution used as an initial guess for the following step.

III. RESULTS

A. Comparison between simulated and experimental data

Sample results for light emission at a constant O_3 inlet concentration of 1300 ppm and flow rates $Q = 250$ and 450 $cm^3\,min^{-1}$, taken from Ref. [6], are shown in Figs. 2(a) and 2(e), respectively. Details regarding the experimental setup are available in Ref. [6]. Also shown are the simulated O_3 partial pressure surfaces at the upper boundary of the catalyst layer domain for each formulation investigated, for the same flow rates. The comparison is qualitative in nature; however, it is seen that all formulations generally agree with the experimental distribution of O_3 at the CL, considering that the apparent reaction rate constant was not available during the simulations.

Specifically, it is seen that the SD formulation overestimates the reactant distribution at lower flow rates [Fig. 2(b)], while maintaining an appropriate correlation at higher values [Fig. 2(f)]. The major differences between the SD formulation and the experimental results seems to occur near the turns of the flow channel, particularly right before and in the y-axis section of the turn. The experimental results show a somewhat abrupt thinning of the reactant distribution when approaching the turn, while the simulated surface shows a continuous decrease along the x-axis section before a turn. Additionally, it is seen that the experimental reactant partial pressure reaches a local minimum in the first corner of each turn, if not slightly before that, while the SD formulation predicts a minimum in the middle of the y-axis section. This is observed even in the first turn, which has no contribution from the crossing of reactant from the previous turns, which suggests it is an effect of the flow field rather than the choice of reaction rate constant.

The DB and SB formulations predict similar surfaces for the O_3 partial pressure distribution to each other, particularly at low flow rates [Figs. 2(c) and 2(d), respectively]. Similarly to the SD formulation, the thinning of the reactant distribution along the x-axis sections of the channel happens continuously, albeit to a lesser extent due to a reduced distribution when compared to the SD formulation. On the other hand, both surfaces show local reactant partial pressure minima near the beginning of each turn, closely resembling the experimental results. When comparing the two formulations, it is seen that the SB formulation shows a larger amount of reactant crossing between

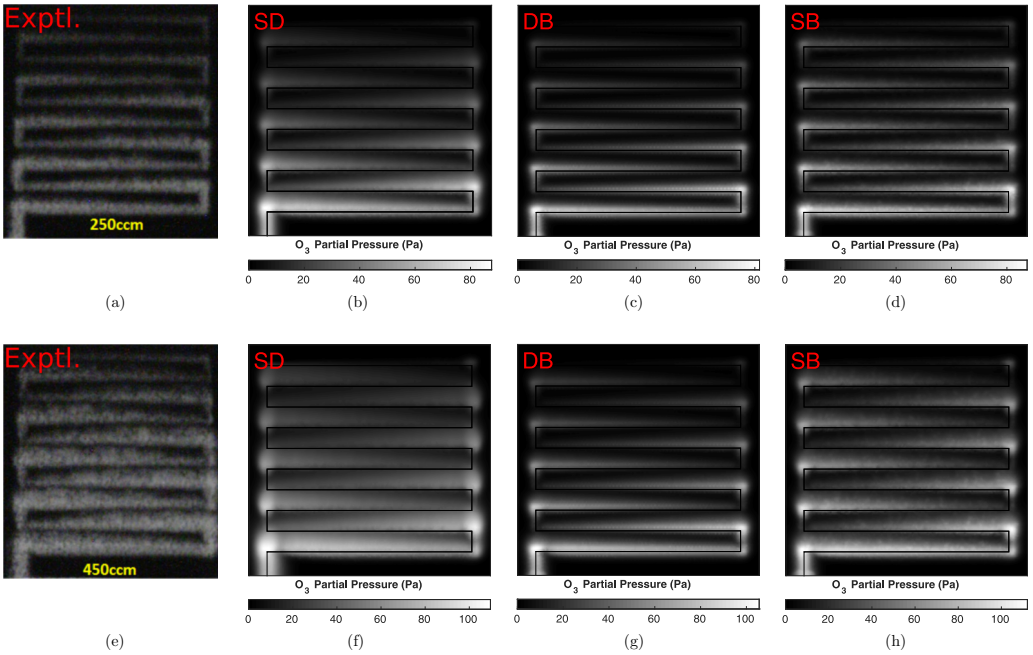

FIG. 2. O_3 partial pressure surfaces, obtained at the upper boundary of the CL, for inlet flow rates $Q = 250$ (top row) and 450 $cm^3\,min^{-1}$ (bottom row): (a), (e) experimental light emission results taken from Ref. [6], with O_3 inlet concentration of 1300 ppm; (b), (f) SD formulation; (c), (g) DB formulation; and (d), (h) SB formulation. Simulated surfaces share an O_3 inlet concentration of 1200 ppm. The line observed in simulated surfaces is the edge indicating the center of the flow channel [see Fig. 1(a)].

turns than the DB one at higher flow rates [Figs. 2(h) and 2(g), respectively]; however, this might be due to the choice of the reaction rate constant.

Figure 3(a) plots the reported and simulated pressure drops against the flow rate. Also indicated, in the top x axis, are the calculated Reynolds numbers. Plotted on the data points are the errors associated with the accuracy of the flowmeter (Omega FMA 3706 mass flowmeter) and differential pressure meter (Digitron 2081P) used in the experiments. It is clear that both the SD and DB formulation results are well within the measurement accuracy, while the SB formulation overestimates the pressure drop. It has been pointed out that the observed slightly higher slope for the SD and DB formulations might be due to the inlet condition used in the model, which is currently that of a normal velocity inflow; however, such a point has not been investigated.

It must be pointed out, once again, that no reported values for the reaction rate constant, k, were found for the O_3-coumarin reaction. The model is based on the hypothesis that the presence of O_3 in the gas mixture should not affect its relevant physical properties, such as density and viscosity, due to the low concentration. However, the rate constant for the O_3-coumarin reaction will have a significant effect on the O_3 partial pressure profile observed in the CL. So in order to fill this gap, as mentioned in Sec. II, the value of k was varied between 10^1 and 10^3 s^{-1} in order to analyze its influence. The resulting partial pressure surfaces are shown in Fig. S5 in the SM, for selected values of k and Q, using all the formulations. It was seen that, as expected from the model's formulation, the fluid flow apparently is not affected by the exact value of k. More important, however, is that the values for k covered in this analysis seem to range from an underestimation to a large overestimation of the reaction rate, at least given the remaining parameters and the comparison to the reported experimental partial pressure surfaces [6]. An in-depth analysis of the best value of k is given below.

The values of total O_3 consumption for the experimental system, not published in Ref. [6], have also been used. Figure 3(b) presents the measured total reactant consumption as a function of inlet

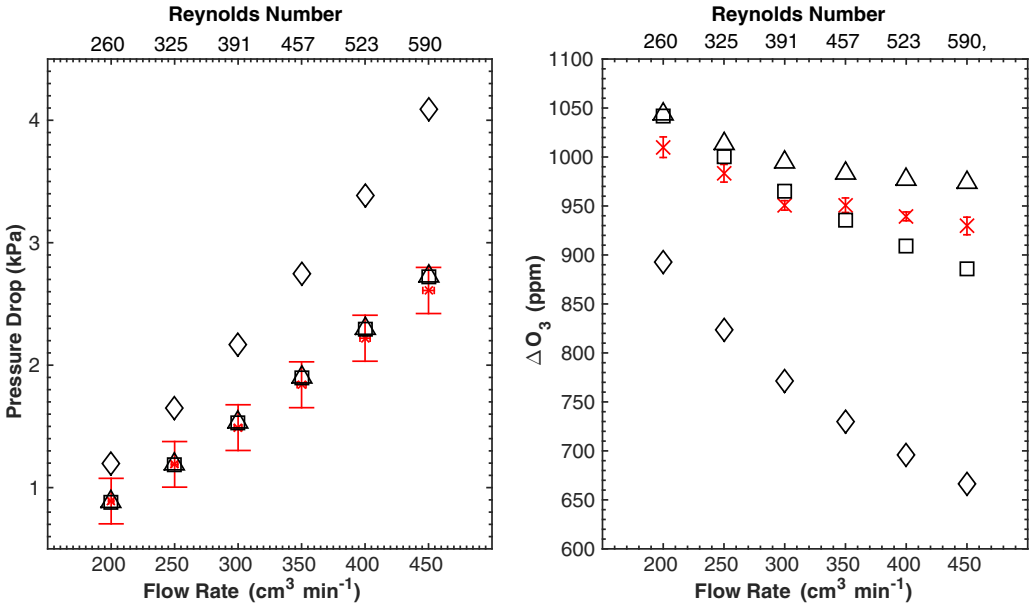

FIG. 3. Global variables as a function of the inlet flow rate, simulated using SD (□), DB (△), and SB (◇) formulations, and the reported measured ones (×). (a) Pressure drop, where the error bars represent uncertainty in the measurements. (b) Total O_3 consumption, where the error bars represent one standard deviation in the measurements.

flow rate, along with the simulated data for each formulation. All simulated values are statistically different from the measured values, although the SD and DB results closely follow the measured values, with the SB formulation presenting a striking deviation from the experimental data. This analysis suggests that, between the SD and DB formulations, the SD formulation is a better fit to the experimental data. Indeed, the mean absolute and maximum errors calculated are, respectively, 25.37 and 31.77 ppm for the SD, and 37.04 and 44.14 ppm for the DB formulation. However, since the total reactant consumption is strongly dependent on the value of the reaction rate constant, such information is unreliable, as the reaction rate constant may be independently adjusted in order to obtain close quantitative agreement with the experimental values. Therefore, one must turn to the qualitative behavior of the response for each formulation. Figure S6 (in the SM) shows a shifted version of Fig. 3(b), where the simulated data sets have been shifted such that the first data points for all data sets overlay. Such an approach makes explicit the differences in behavior between the predictions of each formulation, where it is clear that the slower decline in consumption predicted by the DB formulation more closely agrees with the experimental data. Additionally, the Pearson correlation coefficient was calculated, resulting in 0.9688, 0.9856, and 0.9776 for the SD, DB, and SB formulations, respectively. This may be taken as an indication that the DB formulation may lead to a better predictor for the experimental data, albeit only slightly more so than the other two.

In order to show that the choice of the reaction rate constant is not a major influence on the behavior of the $\Delta O_3 = \Delta O_3(Q)$ curve, Fig. S7 (in the SM) presents additional curves for selected values of the reaction rate constant for each formulation. Some effect of k is observed for high Q values; however, it should be noticed that the values of k span one order of magnitude. Therefore, it should be safe to conclude that the influence of the value of k on the behavior of the curve is weak.

Finally, a closer look at the concentration profiles was attempted. The normalized partial pressure for O_3 was evaluated along the edge present on the upper boundary of the CL and is shown in Fig. 4 for the inlet flow rate of 350 $cm^3\ min^{-1}$. The inset shows the full simulated surface using the DB

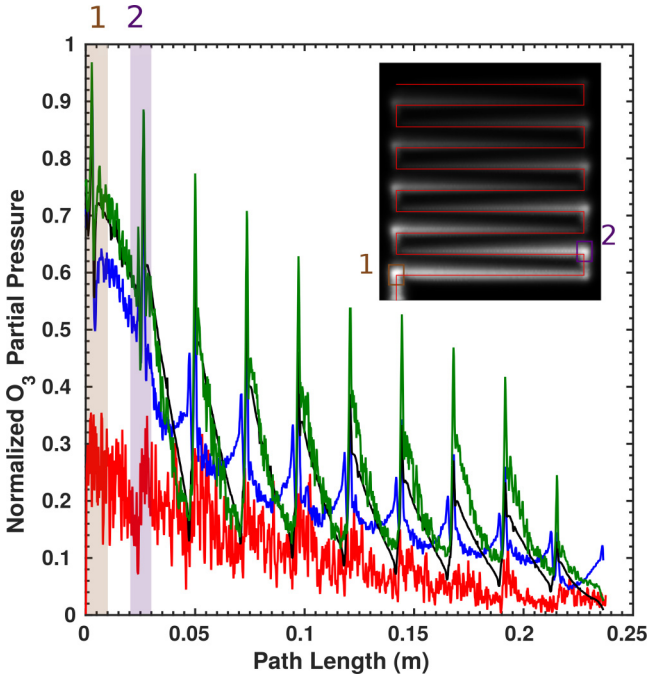

FIG. 4. Normalized O_3 partial pressure evaluated at the upper boundary of the CL, along the middle of the flow channel path, for $Q = 350$ cm^3 min^{-1} (Re ≈ 457). The simulated data, using the SD (blue), DB (black), and SB (green) formulations, are taken exactly along the edge seen in the inset, while the experimental data (red) were taken as the average between the two center pixels roughly along the same path, supplied by the authors of Ref. [6]. Experimental data have been filtered using a low-pass custom filter (details in the text). Inset shows the full simulated partial pressure profile at the CL, with the squares corresponding to the colored sections in the graph, and red line representing the investigated path.

formulation and the edge used for evaluation of the data. Also shown is the average of the two center pixels from the experimental results, supplied by the authors of Ref. [6], roughly along the same path. The experimental data were filtered in order to reduce noise, using a custom low-pass filter (order 5, density factor 20, passband frequency 10 Hz, stopband frequency 100 Hz, sampling frequency 500 Hz, passband weight 1, and stopband weight 5). The data were normalized to their respective maximum value of O_3 partial pressure at the surface. It is clear from the inset, and the respective colored sections in the graph, that the spikes in partial pressure represent the second corner of each turn, while the first spike represents the corner after the inlet. As expected from the general shape of the reactant distribution surfaces shown in Fig. 2, all formulations reproduce the general behavior of the experimental data, mainly the decay and said spikes in partial pressure, and overestimate the near-entrance values. Upon closer inspection, it can be seen that the SD formulation predicts a different behavior for the reactant partial pressure along the x-axis sections of the channel. The experimental data show a somewhat linear decrease along such sections, whereas the SD formulation shows nonlinear behavior, with an increase in local partial pressure before each turn. The DB and SB formulations, on the other hand, seem to correctly predict the linear decrease and sudden jump in partial pressure before each turn.

The difference in behavior seen in the SD formulation could be attributed to the greater degree of reactant crossing between turns of the channel, as seen in the surfaces in Fig. 2. In fact, when using different values of Q and k, such an effect is also observed to a lesser extent in the other formulations, being particularly weak in the DB formulation (see Fig. S8 of the SM [18]). It was seen that the effect of the choice of k in the behavior of the curve is relatively small, as it is in the total reactant

consumption. For instance, in order to more closely correlate the SD formulation to the experimental data, a reaction rate of 500 s^{-1} for low values of Q was needed. However, as is shown in Figs. S5 and S7 of the SM [18], this would lead to an underestimation of reactant distribution and overestimation of total reactant consumption. This constraint points to an effect of the SD formulation's resulting flow field and not of the particular choice of k.

B. Comparison between fluid flow formulations

Given the results and comparisons made above, some points can be drawn with respect to the formulations investigated. First, considering the parametrization described in Sec. II, it is seen that the SD and DB formulations both generally agree with the experimental results, showing both good qualitative and, when possible, quantitative correlation. The SB formulation, on the other hand, showed suitable qualitative results, particularly for the spatial distribution of reactant in the CL (Fig. 2); however, it failed to give correct predictions in the pressure drops and the behavior of the reactant consumption curve [Figs. 3(a) and 3(b), respectively]. Between the SD and DB formulations, the preference would arise from the importance given to each qualitative comparison made, namely, the spatial reactant distribution and the partial pressure behavior along the channel path (Fig. 4). On the other hand, since the number of variables in the SD formulation is smaller, and the different scales of a system are treated separately, it could be argued that the SD formulation is a better choice, being computationally cheaper and as capable as the DB formulation.

Second, considering the constraints that emerged from the analysis of the reaction rate constant, another perspective emerges. It stands that the SB formulation is still inferior, given that the necessary value of k for an adequate reproduction of the total reactant consumption would be greater than 500 s^{-1} (Fig. S7 of the SM [18]), but that would lead to a great underestimation of the spatial distribution of reactant in the CL, even for high values of Q [Fig. S5(i) of the SM [18]]. Even so, the behavior of the total reaction consumption curve would still be inadequate (Fig. S6 of the SM [18]), predicting a faster decline in consumption as a function of Q than the experimental data. For the SD formulation, a similar situation is seen, in which different values of k would be needed to fit the lower and higher Q sections of the reactant consumption curve, albeit only slightly different from the chosen value of 250 s^{-1}. However, it is seen that the behavior of the partial pressure along the channel path differs significantly from the experimental data for such values (Fig. 4), and that values higher than 500 s^{-1} would be needed to minimize such differences (Fig. S8 of the SM [18]). This, in turn, would also lead to a major underestimation of the reactant distribution in the CL [Fig. S5(c) of the SM [18]]. Finally, the DB formulation appears to predict an adequate behavior for the reactant consumption curve, indicating the need for a slightly smaller value for k to actually fit the entire range of Q investigated. Contrary to the other formulations, this would not lead to problems with the remaining data, as the reactant distribution and partial pressure along the channel path are already very close to the experimental data available.

It might be worthwhile, now, to take a closer look at the mathematical framework of the formulations investigated. It has been shown that Eq. (4) can be derived from the Stokes equation using the volume-averaging method [26]. Due to the constraints arising from length scales during the derivation of Darcy's law in Ref. [26], and the fact that the Stokes equation is suitable for creeping flow, one obtains an equation that does not describe inertial or viscous effects. This is readily seen when comparing Eqs. (4) and (3). The DB formulation [Eq. (5)], on the other hand, has been derived directly from the Navier-Stokes equations [11], also using the volume-averaging method, while Ochoa-Tapia and Whitaker [27] show that the so-called Brinkman corrections, present in Eq. (5), can be derived similarly to Darcy's law, i.e., from the Stokes equation. A major difference between the derivations of Eqs. (4) and (5) is that the latter is derived with no length scale constraints, which enables the single equation approach mentioned in Sec. I, since Eq. (5) is valid in all domains throughout the derivation [11,27]. It should also be noticed that, as shown in Ref. [11], Eq. (4) is recovered by taking the low permeability, or large particle diameter, limit of Eq. (5). This corroborates the more general approach given by Eq. (5), despite the approximations used in its derivation.

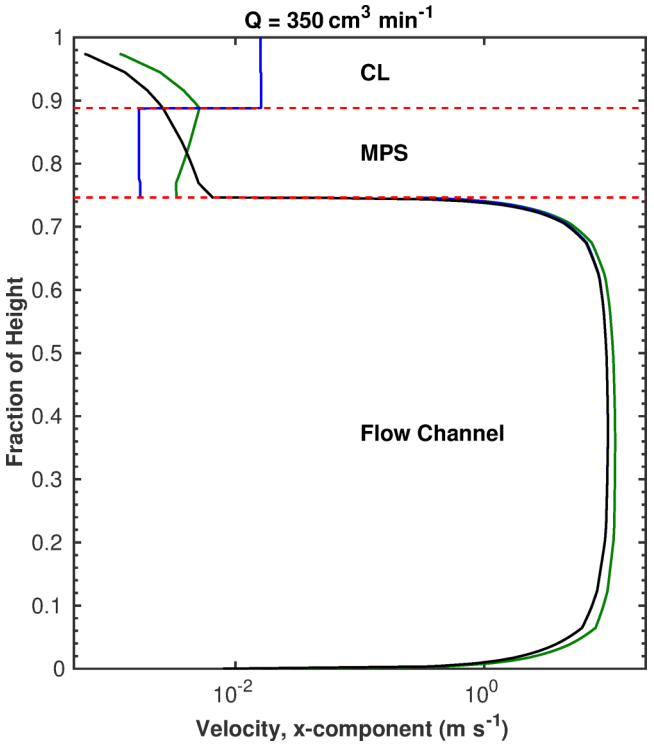

FIG. 5. Profile of the x component of the velocity along the z axis for $Q = 350\ \mathrm{cm}^3\ \mathrm{min}^{-1}$, obtained in the middle of the first horizontal section of the fuel cell: SD (blue), DB (black), and SB (green). The dashed red line indicates the interface between domains.

Taking these into account, it has been mentioned that the lack of viscous effects in Eq. (4) leads to a poor treatment of the interfacial region between free and porous media flow [11,27], hence the need to modify Darcy's law behavior using slip conditions or by extending the domain of validity of the Navier-Stokes equation [11] at the interface. It was discussed in Ref. [11] that an appropriate boundary condition in the SD formulation gives good agreement to the DB formulation, and that the differences scales with the Darcy number $\mathrm{Da} = \kappa/L^2$, where the characteristic length L is usually taken as a slab of the porous medium, in this case 190 μm. This would imply a small influence of the free flow field in the porous medium, described by the thickness of a viscous transition zone $\delta = \sqrt{\mathrm{Da}/\epsilon} \approx 0.02$. This is indicative of how deep the free flow field penetrates into the porous medium, as predicted by the full DB formulation, amounting to approximately the depth at which there is an exponential decrease of the flow field with increasing depth. Hence, the SD formulation should be a good approximation, when coupled to a proper description of the interface. However, a derivation of Darcy's law by Whitaker [26] suggests that the characteristic length might be taken from a representative region of the medium, not necessarily the entirety of the slab. From x-ray microtomography of a similar medium depicted here [24], it can be argued that the length of such a region would be $\sim$50 μm. This leads to a value of $\delta' \approx 0.07$, and considering the exponential decrease of the free flow field, a larger extent is expected, as exemplified in Ref. [11]. Larger errors are expected, then, when using the SD formulation over DB, as shown by Le Bars and Worster. In order to verify the validity of either, a plot of the z-axis profile of the x component of the flow velocity, in the middle of the first section, is shown in Fig. 5. There is evidence of the viscous transition zone reaching as far as 0.16 of the MPS, in accordance with the results of Ref. [11], which indicates that the influence of the free flow field is larger than predicted from the usual calculation of the Darcy number.

Further on, Fig. 5 shows additional features of interest. The DB formulation predicts a nonlinear decay of the flow velocity towards the upper limit of the CL, tending to zero due to the no-slip condition at the boundary. The same is seen for the SB formulation at the CL; however, the transition through the MPS is quite different from the DB, with smaller velocities near the interface and a slow buildup towards the CL, followed by a decay similar to DB. This suggests a reason for the fact that the SB formulation describes the partial pressure surfaces well, while leading to a poor description of the total consumption: the larger flow velocity at the CL compensates for the poor description of the interface of the flow channel with the MPS, due to the boundary conditions used. However, globally, it fails to properly account for the interface effects, ultimately leading to a poor description. On the other hand, for the SD formulation, the expected constant velocity profiles are observed, but it underestimates the flow at the MPS while overestimating it at the CL. This also might explain the observed partial pressure surfaces for the SD formulation, where a greater distribution of reactant is seen when compared to the other two formulations. Figure 5 reiterates that the lack of a proper boundary condition is critical to correctly describe the flow channel–MPS interface in the SD formulation. However, it also raises the issue that the MPS-CL interface should also be properly described, through either a smooth gradient of the transport properties between the materials, or enforcement of the continuity of the velocity.

While more must be done in order to precisely state the origin of the differences between the formulations studied, it is clear that the correct description of interfacial boundary conditions is essential. Considering the system under study, and its proposed ramifications to fuel cells, the use of the SD formulation would be rather elaborate and might be subject to additional errors and uncertainties. This would counterbalance with the advantages of the multidomain approach of the SD, at the same time possibly leading to a poor description of the fluid dynamics. The SB approach might be useful in this regard, when the interfacial region is properly accounted for. However, similar difficulties would remain, and the fact that the DB formulation in principle naturally accounts for these effects tips the balance in favor of the single-domain approach.

Considering the discussion above, and given the parametrization used and the constraints observed in the simulated data compared to the experimental ones, the DB formulation is considered more adequate to reproduce the behavior of the system studied in Ref. [6] and more adequate in its underlying assumptions to further study such a system. Given the intended proximity of this system to fuel cells, particularly devices based on polymer electrolyte membranes, it is tempting to extend such conclusions to these devices. Care should be taken, however, in extrapolating the presented results, as the model encompasses a rather limited range of flow rates and only considers the species transport of a diluted species. It is quite clear that, as suggested by the authors of Ref. [6], the experimental technique developed, and the model presented here, both are representative of the fluid flow in an air-operated fuel cell cathode. However, for reacting mixtures as in fuel cell feeds, the diluted species approach breaks down. Hence, for practical systems, the fluid and especially the species dynamics must be carefully evaluated.

C. Implications for an actual fuel cell

In order to show what the results from Sec. III A would imply in an operating device, a "polarization curve" was created from the models' results. An analogy was drawn using the mathematical framework of electrochemistry, avoiding the introduction of additional variables and uncertainties through a nonvalidated electrochemical model. In the modeled system, there are no activation or ohmic losses; hence, it is not possible to simulate a full polarization curve, as is commonly seen for fuel cells. The system is, on the other hand, constantly under mass-transport limitation. Therefore, it is possible and worthwhile to look at the differences in the concentration overpotential, η_C, given by the different models. It is given by [28]

$$\eta_C = E - E_{\text{eq}}, \tag{13}$$

where E is the electrode potential for a given current, and E_{eq} is the electrode potential at equilibrium, i.e., when no current is flowing. For the modeled system, this can be expressed as

$$\eta_C = \frac{RT}{F}\log\left(\frac{P_{O_3}}{P^*_{O_3}}\right), \tag{14}$$

where R is the ideal gas constant, F is Faraday's constant, P_{O_3} is the local O_3 partial pressure in the CL domain (e.g., Fig. 2), and $P^*_{O_3}$ is the local O_3 partial pressure in the absence of reaction, i.e., disregarding Eq. (8) in the CL domain. Since the O_3 partial pressure is position dependent, an average is taken over the CL domain in order to facilitate analysis. For the current, we consider Faraday's law of electrolysis [28]:

$$I = FA\frac{\partial C_{O_3}}{\partial t}, \tag{15}$$

where A is the effective area for reaction at the CL domain. The right-hand side of the equation can be taken as the volume integral of FR_{O_3}. In this way, the current is given by

$$I = F\int_{CL} R_{O_3}\, dV, \tag{16}$$

where the subscript denotes integration over the CL domain. Finally, taking the definition of R_{O_3} given by Eq. (8),

$$R_{O_3} = -kC_{O_3}.$$

it is noted that the "polarization" can be carried over by varying the reaction rate constant k. The resulting curves for each model and selected inlet flow rates are shown in Fig. 6.

It is noted that, as seen from the results of Sec. III A, both SD and SB formulations overestimate reactant distribution, leading to significantly lower concentration overpotentials for the same current value. No actual new information is shown in Fig. 6; however, the polarization curves sum up the observations presented and discussed before. That is, relative to the best model shown, the DB formulation, the use of SD and SB formulations tends to overestimate fuel cell performance. For instance, with $Q = 350\ \text{cm}^3\ \text{min}^{-1}$ and $k = 250\ \text{s}^{-1}$, the results predict currents $\approx$40% higher with an overpotential $\approx$15% lower for both SD and SB formulations relative to the DB one. For higher currents and flow rates, the difference increases, most notably for the SB formulation. Therefore, it is expected that, for commonly used flow rates and current ranges, the error associated with using the SD formulation will only increase.

Also relevant to fuel cells are the treatment of multicomponent diffusion and the effects of porous media. When the carrier fluid changes composition and is subject to pressure gradients, different driving forces arise due to distinct interactions between the mixtures' components. Meanwhile, when the mean free path of the components is comparable in length to the medium's pore size, collisions with the material become an important effect, leading to the Knudsen regime of diffusion. It is well known that in practical devices, such effects are important and must be taken into account [1], considering that the mixtures are concentrated and change composition along the flow channel, and the mean free path ($\lambda \sim 10^{-7}$–10^{-8} m [29]) and the pore size range of microporous layers used in actual fuel cells ($d_p \sim 10^{-7}$–10^{-8} m [30]). The Knudsen number, $\text{Kn} = \lambda/L$, is a useful indicator of the prevalence of such a regime, where in this case the characteristic length may be taken from the average pore size. When $\text{Kn} \sim 1$, as in the case described above, there are already significant effects due to interactions with the porous material, increasing with Kn [31]. A recent work by Fu and colleagues [32] shows the importance of a detailed treatment of diffusion using the dusty gas model, which incorporates the Maxwell-Stefan model of multicomponent diffusion, the Knudsen regime, and pressure gradients. The authors show that, only by taking into account these different physical processes, a good qualitative comparison with experimental data can be achieved.

While the system under study is designed to be a replica of fuel cells, its conditions allow for approximations to be used. As mentioned before, the use of a diluted, single species diffusion

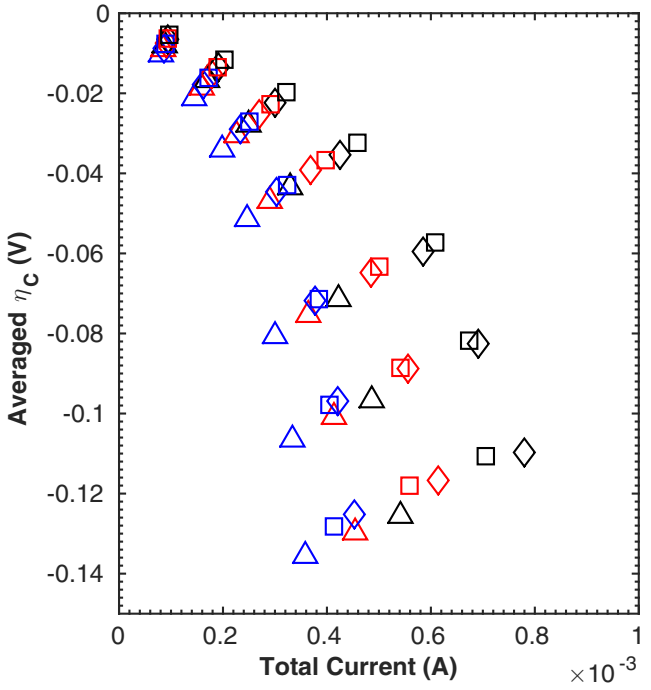

FIG. 6. Averaged concentration overpotential as a function of the total current, defined in Eqs. (14) and (16), respectively, for SD (□), DB (△), and SB (◇) formulations. Inlet flow rate values contemplated: 250 (blue), 350 (red), and 450 $cm^3\ min^{-1}$ (black).

may be justified by the fact that the carrier fluid does not change composition and the tracer concentration being quite low. Regarding Knudsen diffusion, the MPS typically has a pore size range much larger than microporous layers ($d_{MPS} \sim 10^{-5}$–10^{-6} m [33]), while the CL used is very likely to be in a similar range, considering the particle size $\sim 10^{-6}$ and the transport properties obtained from simulations. These values give Kn $\approx 7 \times 10^{-3}$ to 7×10^{-2}, well below the value where molecular diffusion is expected to be significant, and slightly smaller than the one that can be calculated from Ref. [32]. Nevertheless, some tests were carried (see Sec. III of the SM [18]), using the mixture-averaged model, with or without Knudsen diffusion, and the Maxwell-Stefan model, all coupled to the DB formulation. Although not exactly like the dusty gas model described in Ref. [32], it allows for an idea of the scale of these effects, namely, interspecies interactions, the Knudsen regime of diffusion, and pressure gradients. Despite the approximations used for the relevant parameters, when compared to the diluted approach, it is seen that the differences are small, accounting for approximately 30–20 ppm of the total reactant consumption and >10 Pa for the partial pressure surfaces. More importantly, it is seem that the behavior of the curve is basically the same. This corroborates the approximations used in the model; however, it also shows that although the system described by Lopes and colleagues [6] can be used to explore the flow field, it might be rather insensitive to higher order effects such as that discussed above. Further improvements in the experimental setup and computational model should allow the study of such effects.

D. Convective transport in the "gas diffusion layer"

Given the results presented in Sec. III A, and the discussion in Sec. III B, the DB formulation was deemed more appropriate to evaluate the convective transport in the experimental system. Both qualitative and quantitative aspects investigated are appropriately reproduced by the DB formulation,

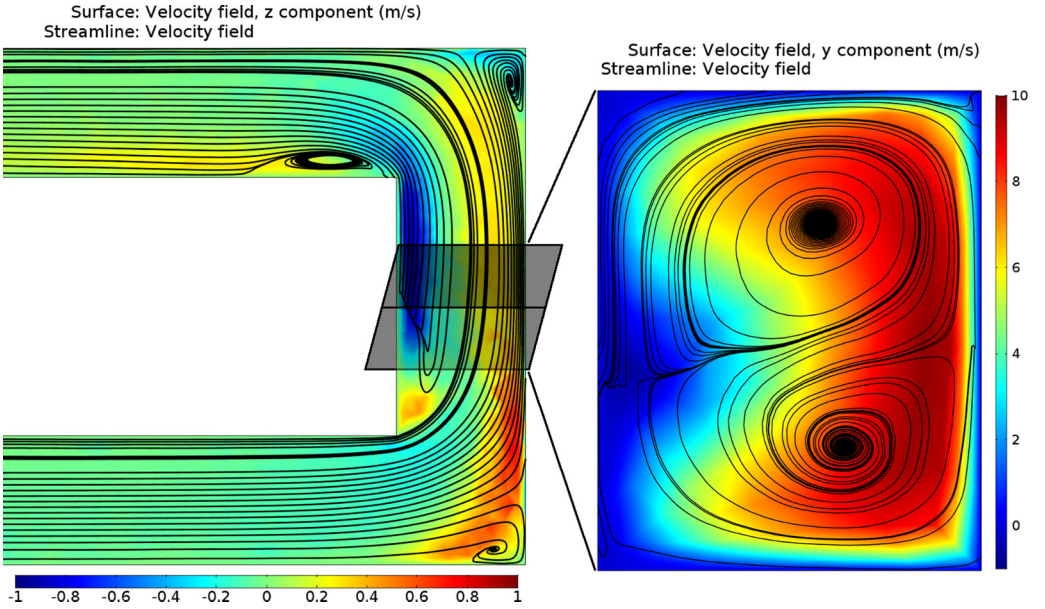

FIG. 7. Flow velocity field in the third turn of the flow channel, for $Q = 350\ \mathrm{cm^3\ min^{-1}}$ (Re ≈ 457). Left: xy cross section through the middle of the channel; color surface represents the z component of the velocity, while the streamlines map the x and y components. Right: xz cross section through the middle of the turn; color surface represents the y component of the velocity, while the streamlines map the x and z components.

and the comparison with the SD and SB formulations indicates that the main reasons for such success are a more suitable description of the bulk fluid flow in porous media and the continuity of the flow field near the interface between free and porous media domains.

We now turn to investigate the proposed contribution of convective transport for reactant distribution in the CL, as reported in Ref. [6]. One point raised by Lopes *et al.* concerns the contribution of secondary flows, in the form of vortices, to the distribution of reactants in the catalyst layer, as have been previously suggested using laser Doppler anemometry in an operating fuel cell [34]. Figure 7 presents the components of the velocity field in the third turn of the flow channel for $Q = 350\ \mathrm{cm^3\ min^{-1}}$ (Re ≈ 457), both in the xy and xz planes. Each surface presents the component of the velocity perpendicular to the plane, with the remaining components as streamlines. From the streamlines the existence of secondary flows is clear, in the form of vortices, and an offset of these velocity components from the center of the flow channels is also clear. The existence of circulation movement in the turn is also seen, as seen in the xz cut, with an upflow of fluid in the upper part of the channel, closer to the MPS, which is consistent with previous results [7]. The information in Fig. 7 correlates with the observed features in the partial pressure surfaces, experimental and simulated, corroborating the idea that secondary flows are important to describe the observed reactant spatial distribution [6].

Secondary flows are, of course, expected for nonideal fluids and finite geometries, though a main concern is the actual contribution to reactant distribution in a device. To investigate this, simulations were performed using a modified model, where the species transport in the porous media is uncoupled from the momentum transport, while still solving for the full flow field; i.e., Eq. (1) becomes the diffusion equation,

$$\nabla \cdot \left(- D_{\mathrm{O_3}} \nabla C_{\mathrm{O_3}} \right) = R_{\mathrm{O_3}}, \tag{17}$$

in the porous media domains. Figure S9 (in the SM [18]) presents the reactant distribution surfaces in the CL. As expected, the reactant partial pressure in the CL is reduced when compared to the

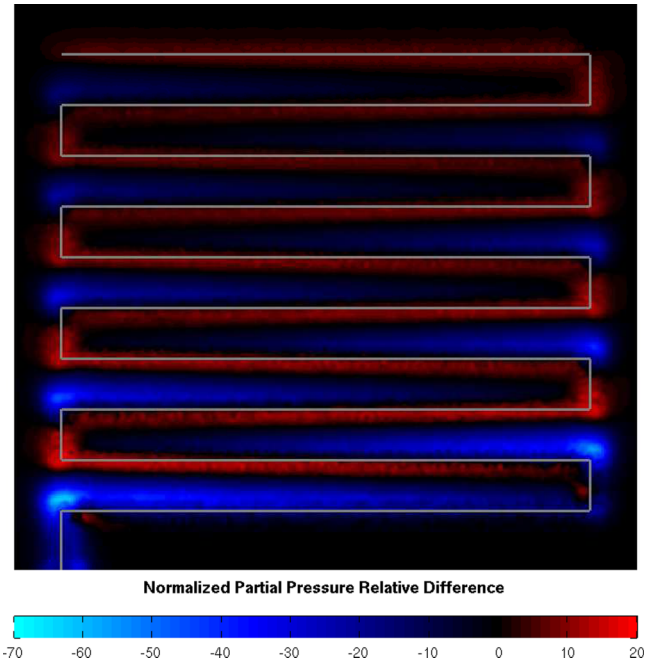

FIG. 8. Normalized difference between the modified and full models' partial pressure surfaces for $Q = 350\ \mathrm{cm^3\ min^{-1}}$ (Re ≈ 457): Blue represents underestimation of the partial pressure by the modified model, while red represents overestimation. Normalization was made using the maximum value at the full model's surface [see Eq. (18)]. The values were taken in a 536×500 grid, with uniform interval of 50 μm. The grey line represents the center of the flow channel.

full model [e.g., Fig. 2(c)], however somewhat constant, despite the increase in inlet flow rate. The most striking result of the modified model is the loss of several features in the reactant distribution when compared to the full model, particularly the ones seen closer to the turns of the flow channel. This is better shown in Fig. 8, where the difference between the modified and full models' partial pressure surfaces is presented for $Q = 350\ \mathrm{cm^3\ min^{-1}}$. The data were generated using a 536×500 rectangular grid. Taking the partial pressure as the matrix $\mathbf{P}$, the surface, $\mathbf{\Delta P}$, was normalized using

$$\Delta P_{ij} = \frac{P_{ij}^{\mathrm{diff}} - P_{ij}^{\mathrm{full}}}{\max(\mathbf{P}^{\mathrm{full}})} \times 100\%, \tag{18}$$

where the max function returns the maximum value of the matrix, and the superscripts diff and full represent the modified and full models, respectively. The color map encodes, in blue, underestimation of partial pressure by the modified model, while red indicates overestimation. As stated above, the major changes observed in the modified model are in sections near the turns, being particularly important after each turn, where the partial pressure is underestimated the most, being reduced to as low as 60%. In the full range of inlet flow rate investigated, it was seen that the partial pressure may reach 110% to 120% times the full model values, mostly in the first corner of each turn, and as low as 40% to 65% near the second corner of each turn. Absolute values aside, Fig. 8 points out the importance of convection in the porous media. Since the model is stationary, one cannot claim that the underestimated effects are those resulting specifically from secondary flows, such as seen in Fig. 7; however, it is quite clear that the crossing of reactant between horizontal sections and turns of the channel is mainly due to convection.

The information presented in Figs. 7 and 8 correlates well with the interpretation of Lopes *et al.* concerning the experimental results reported in Ref. [6]. It is proposed that convection plays a

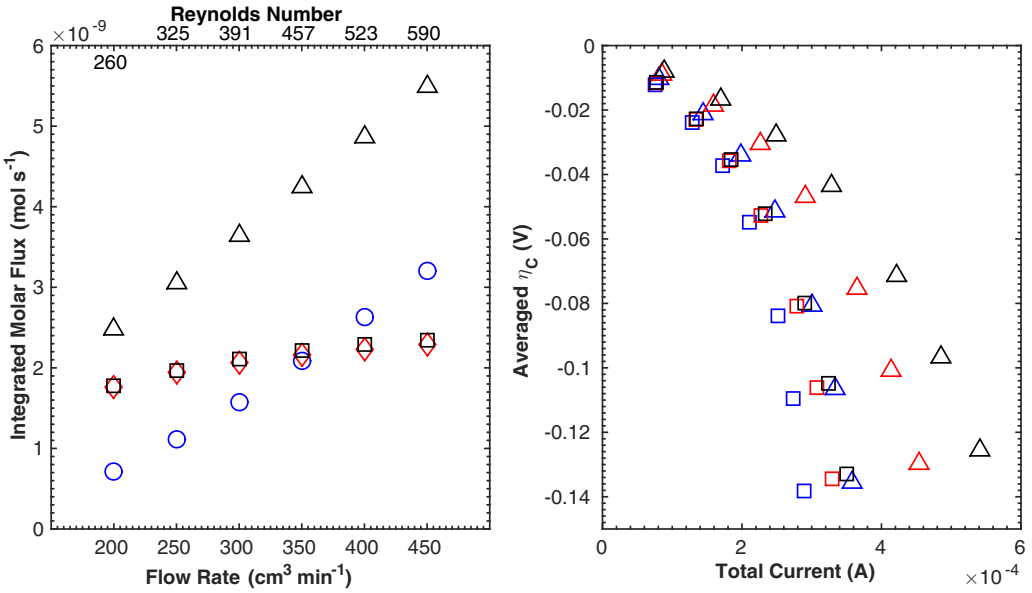

FIG. 9. (a) The z component of the molar flux, integrated over the boundary between the MPS and CL domains, as a function of the flow rate: modified model's total flux (□), and full model's total (△), diffusional (◇), and convective flux (○). (b) Averaged concentration overpotential as a function of the total current, defined in Eqs. (14) and (16), respectively, for full (△) and modified (□) models. Inlet flow rate values contemplated: 250 (blue), 350 (red), and 450 $cm^3\ min^{-1}$ (black).

significant part in the reactant distribution in the porous media, calling for engineering not only flow channels but also the so-called gas diffusion layers, to maximize reactant distribution and, therefore, enhance device efficiency. In this line, an attempt was performed to identify the contribution of convection in the experimental system. A change of slope in the curve of light intensity, proportional to O_3 partial pressure, as a function of inlet flow rate (Re $\approx$ 480) was identified as a saturation of convective transport in the porous media [6]. To verify this, the contributions to the molar flux of reactant to the CL were analyzed. Figure 9(a) presents the z component of each contribution to the molar flux [Eq. (2)], integrated over the boundary between the MPS and CL domains, for both modified and full models. It can be interpreted as the total amount of reactant transported to the CL per unit time, and, as expected, the amount accounted in the full model is significantly higher than that in the modified model. More importantly, though, is the fact that in both models the diffusional contribution, being the total amount in the modified model, is the one presenting an asymptotic behavior, while the convective contribution, in the case of the full model, increases almost linearly over the entire inlet flow rate range investigated. Therefore, contrary to interpretation given in Ref. [6], the convective contribution to reactant transport actually increases throughout the flow rate range (Re = 260–590), amounting from 29% to 58% of the total reactant transport to the CL.

Finally, the same approach of Sec. III C is used to sum up the implications of these findings for an actual fuel cell. Figure 9(b) compares the "polarization curves" of the full and diffusion-only models for selected values of inlet flow rate. It is seen that convection greatly increases the current for similar overpotential values. In particular, for $Q = 350\ cm^3\ min^{-1}$, the contribution of convection ranges from 8.9% to 26.9% for the total current, while decreasing the concentration overpotential from 26.2% to 3.3%. As seen in the figure, this contribution increases with Q, in the same way as seen in Fig. 9(a), playing a significant role in higher values of flow rate. For the ranges of Q and k simulated, this reaches as much as 34.0% of the current, with an overpotential 5.3% smaller.

In a sense, the behavior of the diffusional contribution to the species transport is expected, given that it is driven by the gradient of the reactant's partial pressure, which, in turn, is connected to the catalyst's turnover frequency. Hence, for a given catalyst and operational conditions, the diffusional transport is bound to saturate. On the other hand, the convective transport provides an almost independent contribution to the molar flux, enabling a larger distribution of reactant in the porous media, as seen in Figs. 8 and 9(a), for the same conditions. This reinforces the call for engineering of porous media as well as flow channels, and adds to the possibilities of enhancing fuel cell efficiency by tuning not only water management, but also catalyst distribution coupled to convective transport.

IV. CONCLUSION

Species transport and fluid dynamics in a fuel-cell-like system were studied through a finite element model. The model was validated using data of a unique experimental approach which indirectly measures the reactant's spatial distribution [6], providing valuable information on fluid flow in a system closely resembling a fuel cell cathode in a regime where flooding does not occur. Using an isothermal, diluted species transport approach, the model compared three fluid flow formulations, the Stokes-Darcy, Darcy-Brinkman, and Stokes-Brinkman formulations, with the available experimental data.

The SD and DB formulations were shown to generally agree with the available experimental data, while the SB formulation failed to reproduce the global aspects of the system, i.e., the pressure drop and reactant consumption. An analysis of the constraints of the model, regarding reactant distribution and total consumption, and description of the interface between the flow channel and porous media, led to the choice of the DB formulation as more appropriate to describe the system. It must be noted that the SD formulation is currently taken as the standard approach for fuel cell modeling [1], while the DB formulation seems to lack a proper validation [11] and use in fuel cell modeling, despite having some physical justification for its use. The results and comparison presented in Secs. III A and III B point to the necessity of better descriptions in the porous media flow of fuel cells, while providing a semiquantitative validation of the DB formulation in these systems.

The implication of the differences between formulations observed in Sec. III A were briefly discussed in Sec. III C. A polarization curve analogy was used to compare the concentration overpotential between the studied formulations. It was shown that both SD and SB formulations overestimate fuel cell performance relative to the DB one. The results shown suggest that the error of using simplified mathematical formulations, relative to DB, are bound to increase when considering the usual range of flow rate and currents for commercial fuel cell devices.

The validated model was then used to investigate remarks raised in the experimental work [6]. It has been shown that uncoupling the momentum transfer in the porous media led to a loss of several of the observed features in both experimental and simulated reactants' spatial distribution. This points out that secondary flow does indeed correlate with the observed experimental and simulated phenomena. Furthermore, the results confirm the assertion made in Ref. [6] that, contrary to what is usually assumed, convection provides a major contribution to reactant distribution in the porous layers, from 29% to 58% of total reactant transport to the catalyst layer, in an inlet flow rate range of 200 to 450 $cm^3\,min^{-1}$ (channel Re = 260–590). The diffusive transport shows an asymptotic dependence on the inlet flow rate, while the convective transport shows an almost linear increase over the entire range of flow rate. Using the same approach as in Sec. III C, it is shown that convection significantly increases the current range for similar values of concentration overpotential, reaching 34.0% higher current for 5.3% lower overpotential in the ranges of Q and k simulated.

More work needs to be done, though, in both experimental and computational approaches. Some differences between the measurements are pointed out, and these can be related to the approach used in the model, to under- or overestimating the physical processes, or to experimental uncertainties. Therefore, there is a need to refine both levels, to provide a rigorous comparison between both approaches. At the computational level, electronic structure calculations might provide powerful insights in the catalyst-reactant interaction, which, with an improved mathematical formulation,

might allow for accurate time-dependent simulations, enabling the identification of causal relations in the system. At the experimental level, providing accurate values for the physical properties of the materials used, and exploring the effects of different variables, such as the temperature, should allow for a more rigorous comparison to the model. Improvements of the spatial resolution on both levels is also highly desirable, since it should provide additional information on the finer scale effects that contribute to the overall behavior of the system. On the other hand, the current level does provide some insights, and more studies, e.g., with different channel geometries, may already lead to a solid representation and additional understanding of the system.

Ultimately, the coupling of experimental and computational efforts in modeling a more complex system, in this case fuel cells, is intended to lead to a tool with the capabilities of predicting and optimizing operational design and conditions in the full device.

A file containing the data used to generate the plots in this paper and in the Supplemental Material is available at doi:10.5281/zenodo.889984.

ACKNOWLEDGMENTS

The authors are grateful to the referees for suggestions and pointing out mistakes, allowing for the improvement of the manuscript. O.B. acknowledges a Ph.D. scholarship, Grant No. 2013/11316-9, from São Paulo Research Foundation (FAPESP). O.B. is grateful to Dr. Manuel Cruz and Dr. Harry Schulz for discussions. T.L. acknowledges the Centro Nacional de Desenvolvimento Científico e Tecnológico (CNPq) for support of a postdoctorate fellowship, Grant No. 150249/2014-4, FAPESP for a Young Investigator Awards, Grants No. 2014/22130-6 and 2017/15304-6, and assistance during the writing of the manuscript, Grant No. 2014/09087-4. T.L. would also like to acknowledge the support of the Research Centre for Gas Innovation (RCGI), sponsored by FAPESP, Grant No. 2014/50279-4, and Shell. A.R.J.K. acknowledges funding from the U.K. Engineering and Physical Sciences research council under Grant No. EP/G030995/1, Supergen Fuel Cell Consortium. J.P. acknowledges Grants No. 2011/50727-9 and 2013/16930-7, FAPESP, and Grant No. 311208/2015-0, CNPq.

[1] A. Z. Weber, R. L. Borup, R. M. Darling, P. K. Das, T. J. Dursch, W. Gu, D. Harvey, A. Kusoglu, S. Litster, M. M. Mench, R. Mukundan, J. P. Owejan, J. G. Pharoah, M. Secanell, and I. V. Zenyuk, A critical review of modeling transport phenomena in polymer-electrolyte fuel cells, J. Electrochem. Soc. **161**, F1254 (2014).

[2] A. Z. Weber and J. Newman, Modeling transport in polymer-electrolyte fuel cells, Chem. Rev. **104**, 4679 (2004).

[3] C.-Y. Wang, Fundamental models for fuel cell engineering, Chem. Rev. **104**, 4727 (2004).

[4] K.-D. Kreuer, S. J. Paddison, E. Spohr, and M. Schuster, Transport in proton conductors for fuel-cell applications: Simulations, elementary reactions and phenomenology, Chem. Rev. **104**, 4637 (2004).

[5] M. Bavarian, M. Soroush, I. G. Kevrekidis, and J. B. Benziger, Mathematical modeling, steady-state and dynamic behavior, and control of fuel cells: A review, Ind. Eng. Chem. Res. **49**, 7922 (2010).

[6] T. Lopes, M. Ho, B. K. Kakati, and A. R. J. Kucernak, Assessing the performance of reactant transport layers and flow fields towards oxygen transport: A new imaging method based on chemiluminescence, J. Power Sources **274**, 382 (2015).

[7] A. S. Rawool, S. K. Mitra, and J. G. Pharoah, An investigation of convective transport in micro proton-exchange membrane fuel cells, J. Power Sources **162**, 985 (2006).

[8] F. Barbir, *PEM Fuel Cells: Theory and Practice*, 2nd ed. (Academic Press, Waltham, MA, 2013).

[9] K. W. Knehr, E. Agar, C. R. Dennison, A. R. Kalidindi, and E. C. Kumbur, A transient vanadium flow battery model incorporating vanadium crossover and water transport through the membrane, J. Electrochem. Soc. **159**, A1446 (2012).

[10] W. A. Braff, C. R. Buie, and M. Z. Bazant, Boundary layer analysis of membraneless electrochemical cells, J. Electrochem. Soc. **160**, A2056 (2013).
[11] M. Le Bars and M. G. Worster, Interfacial conditions between pure fluid and a porous medium: Implications for binary alloy solidification, J. Fluid Mech. **550**, 149 (2006).
[12] G. S. Beavers and D. D. Joseph, Boundary conditions at a naturally permeable wall, J. Fluid. Mech. **30**, 197 (1967).
[13] O. Razbani, M. Assadi, and M. Andersson, Three dimensional CFD modeling and experimental validation of an electrolyte supported solid oxide fuel cell fed with methane-free biogas, Int. J. Hydrogen Energ. **38**, 10068 (2013).
[14] L. Valiño, R. Mustata, and L. Dueñas, Consistent modeling of a single PEM fuel cell using Onsager's principle, Int. J. Hydrogen Energ. **39**, 4030 (2014).
[15] COMSOL, COMSOL Multiphysics Reference Manual, 2015, Version 5.1.
[16] COMSOL, CFD Module User's Guide, 2015, Version 5.1.
[17] COMSOL, Batteries & Fuel Cells Module User's Guide, 2015, Version 5.1.
[18] See Supplemental Material at http://link.aps.org/supplemental/10.1103/PhysRevFluids.2.103501 for additional interfacial boundary conditions evaluated for SD and SB formulations; a parametric study of the reaction rate constant value; tests with multicomponent diffusion models; and partial pressure surfaces for the modified, diffusion-only model. References [11,12,19,20,22,23] were used.
[19] R. J. Millington and J. P. Quirk, Permeability of porous solids, Trans. Faraday Soc. **57**, 1200 (1961).
[20] M. L. Huber and A. H. Harvey, Diffusion in gases, in *CRC Handbook of Chemistry and Physics*, edited by J. R. Rumble, 97th ed. (CRC Press/Taylor and Francis, Boca Raton, FL, 2017).
[21] V. Gurau, M. J. Bluemle, E. S. De Castro, Y.-M. Tsou, T. A. Zawodzinski, Jr., and J. A. Mann, Jr., Characterization of transport properties in gas diffusion layers for proton exchange membrane fuel cells 2. Absolute permeability, J. Power Sources **165**, 793 (2007).
[22] R. Ono and T. Oda, Spatial distribution of ozone density in pulsed corona discharges observed by two-dimensional laser absorption method, J. Phys. D: Appl. Phys. **37**, 730 (2004).
[23] W. J. Massman, A review of the molecular diffusivities of H_2O, CO_2, CH_4, CO, O_3, SO_2, NH_3, N_2O, NO and NO_2 in air, O_2 and N_2 near STP, Atmos. Environ. **32**, 1111 (1998).
[24] Z. Fishman, J. Hinebaugh, and A. Bazylak, Microscale tomography investigations of heterogeneous porosity distributions of PEMFC GDLs, J. Electrochem. Soc. **157**, B1643 (2010).
[25] Z. Fishman and A. Bazylak, Heterogeneous through-plane distributions of tortuosity, effective diffusivity, and permeability for PEMFC GDLs, J. Electrochem. Soc. **158**, B247 (2011).
[26] S. Whitaker, Flow in porous media I: A theoretical derivation of Darcy's law, Transport Porous Med. **1**, 3 (1986).
[27] J. A. Ochoa-Tapia and S. Whitaker, Momentum transfer at the boundary between a porous medium and a homogeneous fluid—I. Theoretical development, Int. J. Heat Mass Transfer **38**, 2635 (1995).
[28] A. J. Bard and L. R. Faulkner, *Electrochemical Methods: Fundamentals and Applications*, 2nd ed. (John Wiley and Sons, New York, 2001).
[29] H. V. Kehiaian, Mean free path and related properties of gases, in *CRC Handbook of Chemistry and Physics*, 97th ed., edited by J. R. Rumble (CRC Press/Taylor and Francis, Boca Raton, FL, 2017).
[30] M. V. Williams, E. Begg, L. Bonville, H. R. Kunz, and J. M. Fenton, Characterization of gas diffusion layers for PEMFC, J. Electrochem. Soc. **151**, A1173 (2004).
[31] L. Wu, A slip model for rarified gas flows at arbitrary Knudsen number, Appl. Phys. Lett. **93**, 253103 (2008).
[32] Y. Fu, J. Yi, S. Poizeau, A. Dutta, A. Mohanram, J. D. Pietras, and M. Z. Bazant, Multicomponent gas diffusion in porous electrodes, J. Electrochem. Soc. **162**, F613 (2015).
[33] S. Park, J.-W. Lee, and B. N. Popov, Effect of carbon loading in microporous layer on PEM fuel cell performance, J. Power Sources **163**, 357 (2006).
[34] C. Kalyvas, A. Kucernak, D. Brett, G. Hinds, S. Atkins, and N. Brandon, Spatially resolved diagnostic methods for polymer electrolyte fuel cells: A review, WIREs Energy Environ. **3**, 254 (2014).